Nanoscale

Spatial resolution enhancement in photon-starved STED imaging using deep learning-based fluorescence lifetime analysis

Journal:	*Nanoscale*
Manuscript ID	NR-ART-01-2023-000305.R1
Article Type:	Paper
Date Submitted by the Author:	24-Mar-2023
Complete List of Authors:	Chen, Yuan-I; The University of Texas at Austin, Biomedical Engineering Chang, Yin-Jui; The University of Texas at Austin Sun, Yuansheng; ISS, Inc, Microscopy Liao, Shih-Chu; ISS, Inc. Santacruz, Samantha; The University of Texas at Austin Yeh, Hsin-Chih; The University of Texas at Austin, Biomedical Engineering

ARTICLE

Spatial resolution enhancement in photon-starved STED imaging using deep learning-based fluorescence lifetime analysis

Received 00th January 20xx,
Accepted 00th January 20xx

DOI: 10.1039/x0xx00000x

Yuan-I Chen,*[a] Yin-Jui Chang, *[a] Yuansheng Sun, [b] Shih-Chu Liao, [b] Samantha R. Santacruz, [a,c,d] and Hsin-Chih Yeh *[a,e]

As a super-resolution imaging method, stimulated emission depletion (STED) microscopy has unraveled fine intracellular structures and provided insights into nanoscale organizations in cells. Although image resolution can be further enhanced by continuously increasing the STED-beam power, the resulting photodamage and phototoxicity are major issues for real-world applications of STED microscopy. Here we demonstrate that, with 50% less STED-beam power, the STED image resolution can be improved up to 1.45-fold using the separation of photons by a lifetime tuning (SPLIT) scheme combined with a deep learning-based phasor analysis algorithm termed *flimGANE* (fluorescence lifetime imaging based on a generative adversarial network). This work offers a new approach for STED imaging in situations where only a limited photon budget is available.

Introduction

Super-resolution imaging techniques allow fine structures of subcellular organelles, protein complexes, and membrane domains to be studied in their native environments, revealing new functions of these molecular assembles that were not previously known.[1-4] Among these techniques, stimulated emission depletion (STED) microscopy is particularly suited to image dynamic processes as its light-driven off-switching mechanism well supports a high recording speed.[4-7] STED microscopy keeps the fluorescent molecules within a sub-diffraction volume at an "on" state whilst switching "off" the neighboring molecules (or, more precisely, returning the excited fluorophores back to the ground state without emitting fluorescence) using a donut-shaped depletion laser (i.e., the STED beam).[1, 8] Although the spatial resolution of STED microscopy can be further enhanced by continuously increasing the STED-beam power, it comes at the price of severe photobleaching and phototoxicity.[9, 10] For example, to achieve 50% of probability of returning an excited fluorophore to the ground state within its excited-state lifetime (τ, about 4 ns) using stimulated emission (with energy normalized cross section of 10 cm^2/J), a STED-beam intensity of 25 MW/cm^2 is required.[10] Such an intense excitation either directly damages the live samples or prohibits any long-term observation of the samples.[11]

Several techniques have been developed to maintain or improve the spatial resolution while lowering the STED-beam power.[12, 13] The key lies in reducing the noise in the imaging acquisition process. One source of noise is the anti-Stokes excitation, which can be easily removed by subtracting the STED-beam-only background from the STED images.[14-18] Another source of noise is the "early fluorescence" from the donut-shaped peripheral region.[14] Using a pulsed laser and the time-correlated single-photon counting (TCSPC) scheme, this early fluorescence from the peripheral region can be eliminated by time-gated analysis, creating a method called gated-STED (g-STED) that shows improved STED imaging resolution (**Fig 1a**).[8, 19, 20] However, not limited to the unwanted photons from the peripheral region, g-STED also discards the wanted photons from the central region that arrive at the detector early. As both noise and signal are reduced, the signal-to-noise ratio (SNR) is not necessarily improved.[21]

To differentiate the central fluorescence (signal) from the peripheral fluorescence (noise, due to imperfect depletion), Lanzanò *et al.* developed a method termed SPLIT (separation of photons by lifetime tuning) that integrates a low-excitation-power continuous-wave STED beam (CW-STED) with a phasor strategy to separate photons.[22] Since CW-STED exhibited less depletion efficiency and was more susceptible to the background noise, the continuous-wave depletion beam was later replaced by the pulsed beam (pSTED, **Fig. 1b** and **Fig. S1**).[23, 24] The pSTED-SPLIT method relied on a phasor plot for photon separation, where the decay histogram at each pixel was converted into a phasor point by Fourier transform (**ESI Note 1**).[25] A linear decomposition algorithm was then employed to separate the long-lifetime photons embedded in each phasor point (wanted photons presumably from the center, which is

[a.] *Biomedical Engineering, University of Texas at Austin, Austin, TX, USA.*
[b.] *ISS, Inc., 1602 Newton Drive, Champaign, IL, 61822, USA.*
[c.] *Electrical & Computer Engineering, University of Texas at Austin, Austin, TX, USA.*
[d.] *Institute for Neuroscience, University of Texas at Austin, Austin, TX, USA.*
[e.] *Texas Materials Institute, University of Texas at Austin, Austin, TX, USA.*
† Footnotes relating to the title and/or authors should appear here.
Electronic Supplementary Information (ESI) available: [details of any supplementary information available should be included here]. See DOI: 10.1039/x0xx00000x

denoted as the P_1 phasor component) from the short-lifetime photons (unwanted photons from the periphery, denoted as P_2 phasor component). When the P_1 component was restored and put back to the original scanned image, a STED image with improved resolution was obtained (**Fig. S2**).[26] While SPLIT clearly outperformed g-STED in its imaging quality, the unmixing accuracy of SPLIT was still limited by the shot noise (square root of the number of photons collected at each pixel).[12, 27] Due to the limited photon budgets in imaging biological samples, widely scattered and dislocated phasor points were often seen in a phasor plot, making high-fidelity SPLIT analysis challenging.

To overcome the low-photon-budget issue, we previously developed a deep-learning framework termed *flimGANE* (fluorescence lifetime imaging based on Generative Adversarial Network Estimation) to denoise the time-resolved measurements, generating high-quality fluorescence lifetime images.[28] Here we are combining *flimGANE* with SPLIT, creating a method termed STED-*flimGANE* (**Fig. 1c**) that can achieve an enhanced pSTED imaging resolution under a low STED-beam power (< 30 mW) and photon-starved conditions (< 200 photons per pixel). In addition, our STED-*flimGANE* approach shows minimum dependence of spatial resolution on the STED power. In our method, a GAN model is trained to transform low-photon-count fluorescence decays into highly realistic artificial high-photon-count decays, thus resulting in denoised phasors that can be used to restore fluorophores' true distributions within nanoscale domains. Using our STED-*flimGANE* approach, an average resolution of 64 ± 5 nm is obtained when imaging the 60 nm fluorescent beads (n > 100). We also demonstrate STED-*flimGANE* imaging of nuclear pore complexes (NPCs; having an average size of 60 nm)[29] on COS-7 cells and achieved a spatial resolution of 77 nm. It is verified that STED-*flimGANE* can provide up to 1.45-fold resolution enhancement with less dependence on STED-beam power as compared to the traditional pSTED-SPLIT method.

Materials and methods

The time-resolved pSTED microscope

The time-resolved pulsed STED (pSTED) was implemented on an ISS Alba v5 laser scanning system, which was built either upon a Nikon TE2000 microscope equipped with a 60X NA=1.4 oil objective lens (CFI Plan APO λ, Nikon) for imaging 60 nm fluorescence beads, or a Zeiss Axiovert 200m microscope equipped with a Zeiss Plan-Apochromat 100X NA=1.4 oil objective lens for fixed COS-7 cells. A 642 nm diode laser with pulse duration around 120 ps (QuixX 642-140PS, Omicron-Laserage) and a 775 nm fiber laser with duration around 600 ps (Katana-775HP, NKT Phontonics) were used for fluorescence excitation and depletion, respectively (**Fig. 1b**; **Fig. S1**). A set of Galvo mirrors and a Z-piezo stage (Nano-Z200, Mad City Labs) were employed for 3D scanning of the samples. Both the excitation and the STED lasers were in sync with the lifetime acquisition/analysis module (FastFLIM, ISS), which was triggered at the clock rate of either 50 MHz (for beads samples) or 80 MHz (for biological samples) by the STED laser. The 642 nm laser had a built-in picosecond delayer (10 ps resolution, 0-28 ns tuning range) for precise tuning of the temporal separation between the excitation and depletion pulses. The optimal delay was obtained by comparing the pSTED results of the beads while adjusting the delay in 50-ps steps. The two beams were combined by a 670 nm long-pass dichroic mirror (DM1 in **Fig. 1b**, FF685-Di02, Semrock). A custom-made multi-band dichroic mirror (DM2 in **Fig. 1b**, zt473-491/561/640/2p-trans-pc-uf2, custom-made by Chroma) was used to separate fluorescence emission and stimulated emission and reflect the de-scanned emission light. The fluorescence was collected by an avalanche photodiode (SPCM-ARQH-15, Excelitas), after being filtered by a 720 nm short-pass filter (OD-8 720 nm, Chroma) and a band-pass emission filter (679/41 nm, Semrock). A tuneable and motorized confocal pinhole (with size tuning range from 20 µm to 1 mm) was placed in front of the detector to suppress the background from out-of-focus planes. For the pSTED imaging, the pinhole size was fixed at 50 µm. Photon histograms acquired by the FastFLIM module were converted into a phase plot. A diluted Cy5 solution, with ~1 ns lifetime, was used to calibrate the FastFLIM system before imaging the samples. Each bead or cellular sample was scanned only once with a dwelling time of 0.4 ms per pixel, generating a 512 x 512 image (with an image size of approximately 10.63 x 10.63 µm or 14.64 x 14.64 µm, depending on the location of field-of-view). Data acquisition and a part of the analyses were performed using the ISS VistaVision 64-bit software (**ESI Note 2** and **Fig. S3**). The rest of the analyses (*flimGANE*) were performed in Python.

STED-*flimGANE*

To further enhance the resolution of the pSTED-SPLIT method, the noise of the phasor plot needs to be suppressed and the assignment of the P_1 and P_2 components must be accurate and highly reproducible. To improve the quality of the phasor plot, here we applied the generative adversarial network (GAN) model to denoise the phasors under photon-starved conditions (**Fig. 1c**). The generative model learned to generate realistic objects from noisy inputs *via* an adversarial process.[30] Based on the Wasserstein GAN framework,[31] the generator (*G*) in our *flimGANE* algorithm was trained to produce an "artificial" high-photon-count fluorescence decay histogram based on a low-photon-count input (photon counts < 200 per pixel), while the discriminator (*D*) distinguished the artificial decay histogram from the ground-truth (**Fig. 1c**).[28] Described in more details in **ESI Note 3** and **Fig. S4**, our generator *G* was built on convolutional neural networks (CNN), fully connected neural networks (FCNN), and residual neural networks (ResNet), while the discriminator *D* was comprised of four fully connected layers. To achieve the training goal that maximized the probability of the discriminator making a mistake, the GAN model was trained by minimizing both the generator loss and discriminator loss, which were defined as:

$$G_{loss} = \frac{1}{n}\sum_{i=1}^{n}[-f(G(z_i))],$$

$$D_{loss} = \frac{1}{n}\sum_{i=1}^{n}(-f(x_i) + f(G(z_i))),$$

where z_i represented the i^{th}normalized low-photon-count fluorescence decay histogram, x_i was the i^{th}normalized ground-truth fluorescence decay histogram (obtained by simulations), and $f(x)$ was the 1-Lipschitz function approximated by the discriminative model. In order to avoid mode collapse, a common issue in GAN where the *G* got stuck in a small space with low variety,[31] we included additional loss functions between the generator output and the ground truths (**ESI Note 3**). Eventually, a well-trained *G* enabled the production of very realistic, artificial high-photon-count decays that could be used to generate a robust phasor representation with less scatter in the frequency domain.

As shown in **Fig. 1c**, when the distance of the fluorophore to the center of excitation increased, the depletion effect kicked in and increased the decay rate. The resulting phasor points thus lay along a chord of the G-S semicircle, moving from the top of the semicircle to the lower part of the semicircle, termed a STED trajectory (**Fig. S4**). The two ends of the STED trajectory were the $\boldsymbol{P_1}$ and $\boldsymbol{P_2}$ components, which represented central and peripheral emissions, respectively. Typically, the positions of $\boldsymbol{P_1}$ and $\boldsymbol{P_2}$ were determined manually. To improve accuracy and reproducibility, our STED-*flimGANE* adopted an algorithm to assign $\boldsymbol{P_1}$ and $\boldsymbol{P_2}$ positions in the denoised phasor plot (**ESI Note 4**). In short, we first assigned $\boldsymbol{P_1}$ based on the peak pixels in the *G*-generated S-image. Using beads as the calibration standard, when a bead was 6 pixels away from the center of excitation, the depletion effect reached the maximum. This maximum depletion provided us a threshold (termed $MAX^{0.9}$, where MAX represented the maximum occurrence on the phasor plot; **ESI Note 4**) which could be used to accurately determine $\boldsymbol{P_2}$ location. It was noted that $\boldsymbol{P_1}$ might not lie precisely on the G-S semicircle due to non-zero STED-beam intensity at the central minimum and multi-exponential decay of the fluorophore. Ideally, the phasor point of each pixel would lie along the line of $\boldsymbol{P_1}$ and $\boldsymbol{P_2}$. The fractions of the two components, f_1 and f_2, were then determined *via* linear decomposition.[22] If the phasor point was not right on the line of $\boldsymbol{P_1}$ and $\boldsymbol{P_2}$, it was projected to the line of $\boldsymbol{P_1}$ and $\boldsymbol{P_2}$. Ultimately, given the raw images with *N* acquired photons at each pixel, the final image was reconstructed by putting back only f_1N photons at each pixel. Here we first validated our model using a synthetic dataset (**Fig. S5**-**S7**), followed by applications to real samples (fluorescent beads in **Fig. 2** and biological samples in **Fig. 3**-**4**) under various depletion conditions.

Samples and images acquisition

Two types of samples, 60 nm fluorescent beads and STAR-635P-stained nuclear pore complexes (NPCs) on fixed COS-7 cells, were tested using the STED-*flimGANE* method. The beads were first diluted in water and sparsely coated on a poly-L-lysine-treated glass coverslip. The fixed COS-7 cells were stained with a primary antibody against the nuclear pore complex protein Nup 153 and then a secondary antibody conjugated with STAR-635P. The power of the 642 nm laser for fluorescence excitation was fixed at 2.2 μW (measured at the back aperture of the objective), while the power of the 775 nm depletion beam varied for spatial resolution investigation.

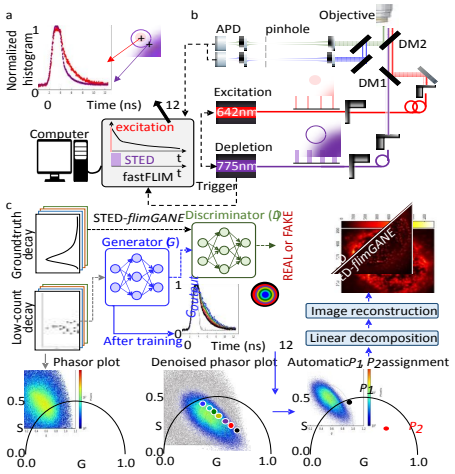

Fig. 1. Principle of the STED-*flimGANE*. (a) The temporal dynamics of fluorescence can be used to improve the STED imaging resolution. When the distance of a fluorophore to the center of excitation increases, the depletion effect kicks in and increases the decay rate. (b) pSTED microscopy setup uses a pulsed excitation and pulsed depletion beam (i.e., the STED beam). The two laser beams are combined by a dichroic mirror (DM1), forming diffraction-limited Gaussian (red) and doughnut-shaped focal intensity distribution (purple), respectively. The fluorescence (green and blue) is detected by the avalanche photodiodes (APDs) and registered by a digital-frequency-domain lifetime acquisition module. (c) Our STED-*flimGANE* method integrates the SPLIT (separation of photons by lifetime tuning) scheme with a deep learning-based phasor analysis algorithm termed *flimGANE* (fluorescence lifetime imaging based on a generative adversarial network) to improve the STED imaging resolution while using a lower STED-beam power. The well-trained STED-*flimGANE* model can generate a robust phasor representation (*G*-generated phasor plot) with less scatter for reconstructing STED images with higher spatial resolution.

Results

Synthetic data and the STED-*flimGANE* model training

The STED-*flimGANE* model was first trained using a Monte Carlo simulation dataset (**Fig. S5** and **ESI Note 5**). A Python program was employed to simulate the photon collection process in the counting device with either 64- (for fluorescent beads) or 256-time bins (for stained NPCs), followed by the probability mass function calculation based on the convolution of an experimentally obtained instrument response function (IRF) and a theoretical fluorescence decay in the

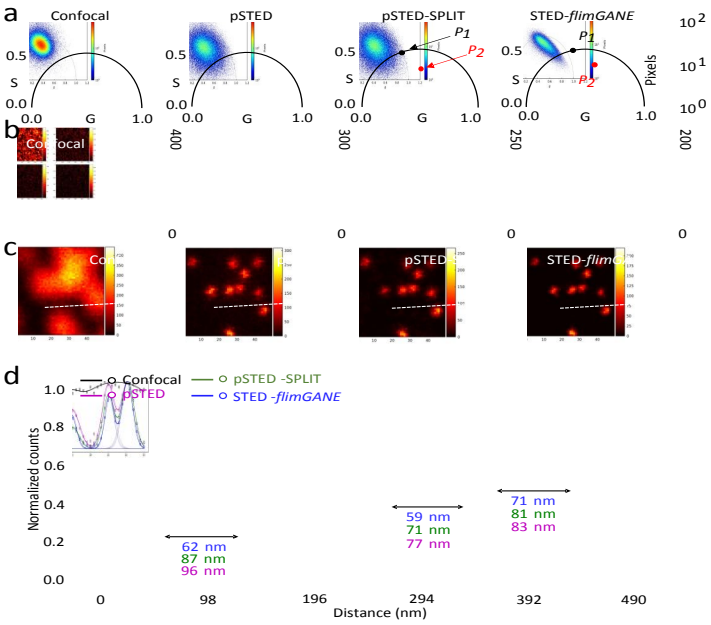

Fig. 2. Fluorescent bead imaging results using confocal, pSTED, sSTED-SPLIT and STED-*flimGANE* microscopy. (a-b) The phasor representations (a) and the intensity images (b) of the confocal, pSTED, pSTED-SPLIT, and STED-*flimGANE* images for 60 nm fluorescent beads. The STED-beam power (P_{STED}) was fixed at 120 mW. Scale bars, 1 µm. (c) Zoom-in views of the box regions in (b) showed that the STED-*flimGANE* achieved the highest spatial resolution. Scale bars, 400 nm. (d) Line profiles of the confocal, pSTED, pSTED-SPLIT, and STED-*flimGANE* images in (c). A two-component Gaussian fitting was utilized to obtain the FWHM of the fluorescent beads. The average resolutions are 75 ± 5, 70 ± 6 and 64 ± 5 nm (n = 125) for pSTED, pSTED-SPLIT and STED-*flimGANE* microscopy, respectively.

central and peripheral regions, generating the following piecewise function:

$$I_i(t) \propto \begin{cases} e^{-t/\tau_{i,STED}} & \text{if } 0 \le t < T_{STED} \\ e^{-T_{STED}/\tau_{i,STED}} e^{-(t-T_{STED})/\tau_{i,fl}} & \text{if } t \ge T_{STED} \end{cases}$$

Where I_i represented the intensity at time t and location i, $\tau_{i,fl}$ represented the natural fluorescence lifetime of a fluorophore at location i, $\tau_{i,STED}$ was the shortened fluorescence lifetime under the STED-beam depletion at location i, and T_{STED} was the STED-beam pulse duration (600 ps in this work). Location i = 1 represented the center while i > 1 indicated the (i -1) pixels toward the periphery. Depending on the fluorophores that users wanted to image (0.5-3.5 ns for natural fluorescence lifetime of most fluorophores) and the available photon budgets (50-5,000 photon counts per pixel), 300 normalized ground truths and 150,000 degraded decays were generated for training *G* and *D*. The adversarial network training was completed in 2.3 hours.

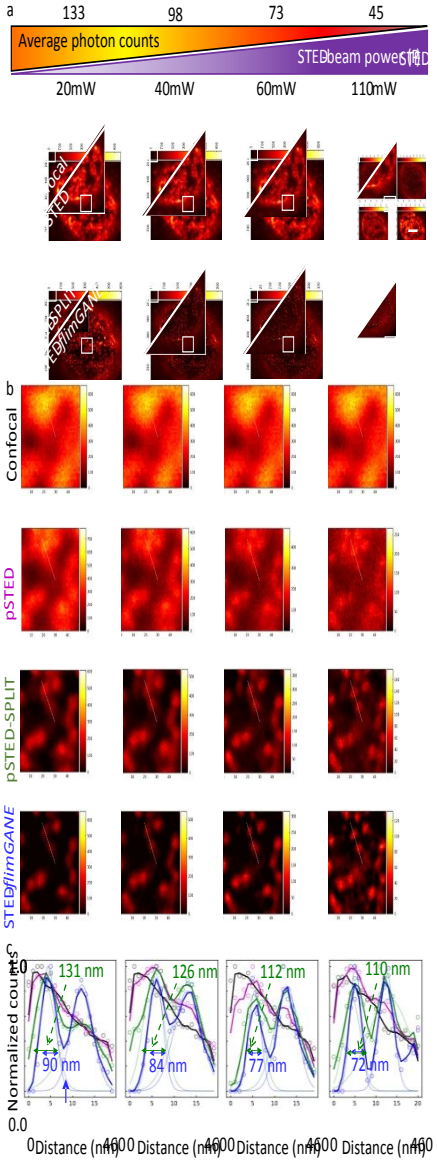

Fig. 3. Nuclear pore complex (NPC) imaging results on COS-7 cells under low-to-medium depletion power conditions. (a) The intensity images of NPCs using the confocal, pSTED, pSTED-SPLIT, and STED-*flimGANE* microscopy under various depletion powers. COS-7 cells were stained with a primary antibody against Nup 153 and a STAR-635P-labeled secondary antibody. Scale bars, 1 µm. Colormap ranges were provided in **Table S1**. (b) Zoom-in views of the box regions in (a) showed that only the STED-*flimGANE* could well resolve the two adjacent nuclear pore complexes (indicated by white dashed lines) at P_{STED} = 20 mW. Scale bars, 200 nm. (c) Line profiles of the confocal, pSTED, pSTED-SPLIT, and STED-*flimGANE* images in (b). The average resolutions are 116 ± 1 and 101 ± 1 nm (n = 100) for pSTED-SPLIT and STED-*flimGANE* microscopy, respectively, at P_{STED} = 20 mW.

The normalized degraded decay was transformed into the normalized "ground-truth mimicking" histogram, termed G_{output}, within 0.08 ms per pixel. After the training process, G_{output} became indistinguishable by *D* from the ground truth dataset (**Fig. 1c** and **Fig. S6**).

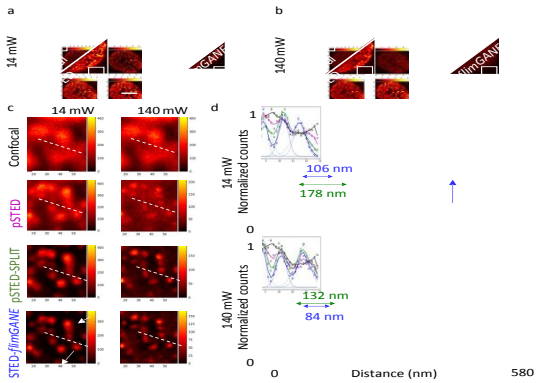

Fig. 4. Nuclear pore complex (NPC) imaging results on COS-7 cells at extreme depletion power conditions. (a) The intensity images of the confocal, pSTED, pSTED-SPLIT, and STED-*flimGANE* for the STED probe under extremely low depletion conditions (P_{STED} = 14 mW). Scale bars, 1 µm. Colormap ranges were provided in **Table S1**. (b) The same as (a) but under extremely high depletion conditions (P_{STED} = 140 mW). (c) Zoom-in views from the solid box region in (a, b) demonstrated that the STED-*flimGANE* achieved a similarly high spatial resolution using extreme depletion power. Obvious improvements were observed from extremely low to high depletion for both pSTED and pSTED-SPLIT. Scale bars, 400 nm. The arrows indicated that only STED-*flimGANE* was able to resolve the closely packed NPCs under extremely low depletion conditions. (d) Line profile of the confocal, pSTED, pSTED-SPLIT, and STED-*flimGANE* images in (c).

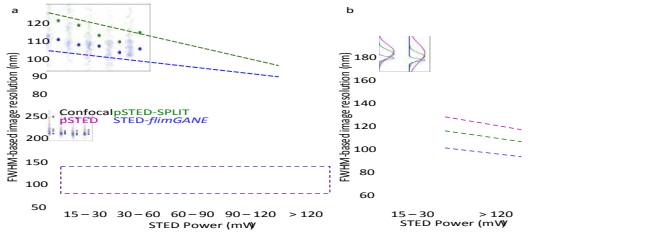

Fig. 5. The STED-*flimGANE* provided reliable super-resolution images across various STED depletion conditions. (a) Qualification of the resolution in the confocal, pSTED, pSTED-SPLIT, and STED-*flimGANE* images. The optical resolution was determined by the FWHM of the intensity profiles of the nuclear pores. STED-*flimGANE* exhibited 50% less dependency of the image resolution on the STED power. The transparent points in the raincloud plots represented individual FWHM values for 100 randomly selected NPCs while the darker points represent the average FWHM values from Gaussian fitting. (b) The fitted Gaussian distributions of pSTED, pSTED-SPLIT, and STED-*flimGANE* on the FWHMs under two P_{STED} conditions: 15-30 mW and >120 mW depletion power.

Two validation steps were employed to evaluate the accuracy and reliability of the STED-*flimGANE* imaging. First, success in training was reflected by the quick drop of training loss (mean-squared error, MSE; **Fig. S6a**), followed by the convergence to 0.01 count^2 after training iterations. Second, Sarmento *et al.* evaluated the SNR of a phasor plot based on the spread along the direction of the phasor elongation. Adopting the same strategy, we assessed the denoising performance of our STED-*flimGANE* algorithm (**ESI Note 6**).[32] When tested on an unseen dataset, STED-*flimGANE* showed 2.9-, 2.2-, and 2-fold improvement in SNR of the denoised phasor plots as compared to the plots before denoising, for the ultra-low- (< 100 photons per pixel), low- (100-200 photons per pixel), and medium-photon-count (200-300 photons per pixel) conditions, respectively, and a positive correlation (0.95; Pearson correlation coefficient) between the model performance and the SNR (**Fig. S7**). These metrics verified that the STED-*flimGANE* is a reliable model for STED imaging analysis and reconstruction.

Validation of STED-*flimGANE* using 60 nm fluorescent beads

When imaging fluorescent beads, the power of the 775 nm depletion beam was fixed at 120 mW. Under such a strong STED-beam power, the acquired average photon count per pixel reduced to 41 photons (**Fig. 2** and **ESI Note 7**). In the confocal imaging (equivalent to STED imaging without the depletion beam), the phasors mapped from all pixels scattered around the long lifetime (P_1) components in the semicircle. In contrast, when the STED beam was employed, the phasor distribution elongated toward the short lifetime (P_2) component (**Fig. 2a**). The formation of a clear STED trajectory clearly facilitated photon separation in the pSTED-SPLIT and STED-*flimGANE* schemes, thus improving the spatial resolution (**Fig. 2b-c**). By fitting the line profiles with a multi-peak Gaussian function (**Fig. 2d** and **ESI Note 8**), we estimated the full-width-at-half-maximum (FWHM) of these fluorescent beads (n > 100) to be 64 ± 5 nm when using STED-*flimGANE*, which was 1.17-fold and 1.09-fold improvement as compared to the conventional pSTED imaging (75 ± 5 nm) and the pSTED-SPLIT imaging (70 ± 6 nm), respectively.

Performance of STED-*flimGANE* in imaging biological samples

When imaging nuclear pore complexes (NPCs, with an average size of 60 nm) on fixed COS-7 cells, STAR-635p was used as the STED dye that stained nucleoporin Nup 153 through a primary and a secondary antibody (**Fig. 3a-b**). As expected, with a more effective algorithm to separate unwanted photons, STED-*flimGANE* outperformed pSTED, and pSTED-SPLIT in resolving NPCs under low-photon-count (133 average photons per pixel) to ultra-low-count (45 average photons per pixel) conditions (**Fig. 3c**). Both pSTED and pSTED-SPLIT schemes failed to

reconstruct a clear NPC image at a low STED-beam power (20 mW) and high average photon count (133 per pixel), indicating a reduced resolution due to the early fluorescence background. However, under this low depletion condition, STED-*flimGANE* still well resolved the adjacent NPCs (**Fig. 3b**). The line profile from the STED-*flimGANE* image exhibited a clear trough between the adjacent NPCs (**Fig. 3c**). When the distance between adjacent NPCs was down to 140 nm, only STED-*flimGANE* could better differentiate these NPCs (**Fig. S8**). In contrast, pSTED and pSTED-SPLIT could resolve the same pair of NPC only when the STED-beam power was higher (≥60 mW). Although the resolution of the STED-*flimGANE* slightly improved under high STED-beam power (**Fig. 3c**), its spatial resolution dependence on the STED-beam power was much less than that of pSTED and pSTED-SPLIT. Specifically, the STED-*flimGANE* showed 1.45-fold improvement in spatial resolution (77 nm) as compared to that of pSTED-SPLIT (112 nm) under the STED-beam power of 60 mW, indicating that STED-*flimGANE* could further enhance the spatial resolution when STED-beam power was kept low.

Resolution comparison under extreme depletion power conditions

Here we compared the spatial resolution of the STED-*flimGANE* imaging with that of the confocal, pSTED, and pSTED-SPLIT imaging under extremely low (P_{STED} = 14 mW, 120 average photons per pixel) and extremely high (P_{STED} = 140 mW, 55 average photons per pixel) depletion power conditions (**Fig. 4a-b**). As expected, the $\boldsymbol{P_2}$ component moved closer to (1, 0) under the high depletion power (**Figs. S9-10**). Although both pSTED-SPLIT and STED-*flimGANE* could differentiate closely packed NPCs under the high depletion power, some closely packed NPCs were not resolved in pSTED-SPLIT imaging under the low depletion power (**Fig. 4c-d and Fig. S11**). In contrast, STED-*flimGANE* well resolved these closely packed NPCs even under a low depletion power. In addition, STED-*flimGANE* offered more background suppression in the surroundings of the NPCs and the outer regions of the cells (**Fig. 4c**).

Evaluation of the spatial resolution dependence on STED power

Using as the resolution estimate, FWHM of the point spread function was determined by fitting the intensity profiles of 100 randomly selected NPCs with a Gaussian function (**Fig. 5**), where the FWHM was equal to 2.35σ. Under all STED-beam powers used in this investigation, STED-*flimGANE* not only achieved super resolution imaging (i.e., FWHM < 200 nm, **Fig. 5a**), but showed 1.13-fold improvement in spatial resolution (on average) over the traditional pSTED-SPLIT imaging. When the same resolution was maintained, STED-*flimGANE* only required one-fourth the depletion power as compared to pSTED-SPLIT (30 mW vs. 120 mW). While the resolution of both methods could be enhanced by increasing the STED-beam power, STED-*flimGANE* clearly showed less dependence on the depletion power (the slope of the linear regression fit was only half of that of the pSTED-SPLIT fit). In addition, the FWHM distributions also indicated STED-*flimGANE* had less dependence on the STED-beam power (**Fig. 5b**). All these results suggested that STED-*flimGANE* is a better form of the SPLIT method and is more suitable for imaging live samples (although here we only tested STED-*flimGANE* on fixed cells).

Discussion

In this work, we have demonstrated that the STED-*flimGANE* can achieve 77 nm lateral resolution in imaging nuclear pore complexes on fixed COS-7 cells, under the conditions of 73 photons per pixel and 60 mW STED-beam power. These results indicated that the STED-*flimGANE* is a robust, fit-free and user-friendly method for enhancing the spatial resolution with minimum dependence on the STED-beam power, even in the presence of uncorrelated background and shot noise. The denoising capability of the STED-*flimGANE* on the noisy fluorescence decays *via* GAN is the key to providing robust phasor representations for downstream photon separation (**Fig. S6**). Although GAN-based approaches have been used to transform the confocal images to match the resolution of STED images,[33, 34] to the best of our knowledge, this is the first report that the GAN is applied to improve the spatial resolution of STED imaging based on the fluorescence temporal dynamics.

It is worth noting that STED-*flimGANE* maintains good spatial resolution even when photon counts are low. Insufficient photons result in scattered phasor points in the phasor plot, leading to so-called scatter error.[35] Since the scatter error scales inversely with the square root of the total photon counts per pixel, filtering is a typical strategy to denoise phasor plots under photon-starved conditions. For instance, a median filter is commonly used for phasor denoising;[36] however, high-spatial-frequency components such as the edge of features are often diminished.[37] To preserve these high-frequency components, STED-*flimGANE* employs Wasserstein distance as the loss function, which provides a smoother gradient for GAN network training under all conditions (**ESI Note 3**). As a result, the well-trained generator in STED-*flimGANE* seamlessly converts low-photon-count decays into highly realistic high-photon-count ones, leading to a denoised phasor plot with much less scatter error.[28] Although other strategies such as the complex wavelet transform methods can also preserve fine structures and concurrently clean up noisy images,[37, 38] they require additional steps, such as selection and optimization of the basis functions, before the transformation.

A few reports demonstrated low-power STED imaging through modulating the STED beam. One example is the adaptive STED-illumination strategy DyMIN (Dynamic intensity MINimum) that provides the imaging of NPCs at a resolution of 73 nm with 30 and 344 mW STED-beam powers for two cycles.[18] Similarly, modulation-enhanced STED (M-STED) also achieves 87 nm resolution of NPCs by analyzing the STED trajectory under various STED-beam powers.[32, 39] However, changing the STED-beam power not only increases the data acquisition time but also complicates the analysis process. In contrast, our STED-*flimGANE* only relies on post-processing, which provides a comparable resolution without the need of spending additional time modulating the STED-beam power. We emphasize that this method is simple to implement in the existing optical system

such as modulated STED (mSTED) to facilitate the observation of the rapid process of the biological samples.[40] Although the network training time may be the bottleneck for STED-*flimGANE*, this issue can be overcome by using more advanced hardware (e.g., graphic processing unit or tensor processing unit) or transfer learning techniques that take advantage of the previously trained networks.[41]

The STED-*flimGANE* is a versatile and efficient method for improving the resolution of STED microscopy, which can be easily adapted on a variety of standard and custom setups. Bayesian optimization provides an efficient means to select the optimal hyperparameters. The $\boldsymbol{P_1}$ and $\boldsymbol{P_2}$ phasor components in the traditional SPLIT are either assigned manually or determined by the characteristic limits of the operative range. As a result, these phasor components can be skewed due to bias, or require recalibration once the sample or the excitation/depletion power is changed. In contrast, STED-*flimGANE* automatically assigns the $\boldsymbol{P_1}$ and $\boldsymbol{P_2}$ phasor components without the need of recalibration, thus eliminating any user or experimental bias. Similar to the existing photon-separation approaches, we expect STED-*flimGANE* to be capable of improving the resolution in both CW and pulsed STED. While the implementation of CW-STED is more straightforward, less depletion efficiency and more susceptibility to the background noise limit its widespread use in various applications.[12, 42, 43] Here we demonstrate STED-*flimGANE* using pSTED, achieving up to 1.45-fold improvement in spatial resolution under the conditions of both 20 mW (90 nm vs 131 nm) and 60 mW (77 nm vs 112 nm) STED-beam power (**Fig. 3c**). The higher STED-beam power depletes more photons from the periphery at the expense of SNR of the phasor plot (**ESI Note 6** and **Fig. S8**). In contrast, the lower STED-beam power yields a better quality of phasor plot, but at the cost of the spatial resolution. As live-cell imaging usually involves a compromise between image quality and cellular health, the labeling protocols and imaging conditions are required to be optimized according to the users' purpose.[4]

Conclusions and Outlook

Here we introduce a new method termed STED-*flimGANE* (combination of a deep learning-based phasor analysis, fluorescence lifetime imaging based on Generative Adversarial Network Estimation, and the separation of photons by lifetime tuning scheme) that can achieve enhanced STED imaging resolution under a low STED-beam power (< 30 mW) and photon-starved conditions (< 200 photons per pixel). Our STED-*flimGANE* method can rapidly generate robust phasor representations with less scatter error. Images reconstructed by these denoised phasor plots clearly show improved resolution and quality. Our work represents an important step towards low-power STED imaging for live-cell or live-tissue imaging applications, allowing users to achieve desired spatial resolution without significantly causing phototoxicity and photodamage to the samples. Our next task is to demonstrate STED-*flimGANE* in imaging organelles in live cells. As one of the key advantages of phasor analysis is the differentiation of multiple fluorophores with different lifetimes excited by a single excitation source,[44, 45] with recent development in fluorescence lifetime tuning strategies in fluorophores and protein tags,[46-49] we envision that our STED-*flimGANE* can also be adapted for multiplexed STED imaging.

Author Contributions

Y.-I.C., Y.-J.C., and H.-C.Y. conceived the project and wrote the article. Y.-I.C., and Y.-J.C. developed image processing and analysis software. Y.-I.C. and Y. S. designed the experiments. Y.-I.C., Y. S., and S.-C.L. prepared samples and collected images. Y. S. and S.-C.L. supported the instrumental setup for all experiments. H.-C.Y. and S.R.S. advised the experimental designs and data analysis. Y.-I.C. and H.-C.Y. supervised the project. All authors have given approval to the final version of the manuscript. *These authors contributed equally.

Conflicts of interest

Y. S. and S.-C.L. are employees of ISS Inc., a company commercializing microscopes.

Acknowledgments

The authors thank Dr. Beniamino Barbieri from ISS Inc. for the inputs and discussions. Y.-I.C. especially thanks Dr. Che-Ming (Jack) Hu from Academia Sinica for the inspiration of this project. This work is supported by NSF (2029266), the Welch Foundation (F-1833), NIH (GM129617 and EY033106), and Texas 4000 Foundation. Y.-I. C. is supported by the Texas Health Catalyst Program at Dell Medical School.

Notes and references

1. S. W. Hell and J. Wichmann, *Optics Letters*, 1994, **19**, 780-782.
2. E. Betzig, G. H. Patterson, R. Sougrat, O. W. Lindwasser, S. Olenych, J. S. Bonifacino, M. W. Davidson, J. Lippincott-Schwartz and H. F. Hess, *Science*, 2006, **313**, 1642-1645.
3. M. J. Rust, M. Bates and X. Zhuang, *Nature Methods*, 2006, **3**, 793-796.
4. S. J. Sahl, S. W. Hell and S. Jakobs, *Nature Reviews Molecular Cell Biology*, 2017, **18**, 685-701.
5. V. Westphal, S. O. Rizzoli, M. A. Lauterbach, D. Kamin, R. Jahn and S. W. Hell, *Science*, 2008, **320**, 246-249.
6. J. Schneider, J. Zahn, M. Maglione, S. J. Sigrist, J. Marquard, J. Chojnacki, H.-G. Kräusslich, S. J. Sahl, J. Engelhardt and S. W. Hell, *Nature Methods*, 2015, **12**, 827-830.
7. S. Calovi, F. N. Soria and J. Tønnesen, *Neurobiology of Disease*, 2021, **156**, 105420.
8. S. W. Hell, *Nature Methods*, 2009, **6**, 24-32.
9. P. P. Laissue, R. A. Alghamdi, P. Tomancak, E. G. Reynaud and H. Shroff, *Nature Methods*, 2017, **14**, 657-661.
10. G. Vicidomini, P. Bianchini and A. Diaspro, *Nature Methods*, 2018, **15**, 173.
11. N. Kilian, A. Goryaynov, M. D. Lessard, G. Hooker, D. Toomre, J. E. Rothman and J. Bewersdorf, *Nature Methods*, 2018, **15**, 755-756.

12. Y. Ma and T. Ha, *Physical Biology*, 2019, **16**, 051002.
13. P. Gao, B. Prunsche, L. Zhou, K. Nienhaus and G. U. Nienhaus, *Nature Photonics*, 2017, **11**, 163-169.
14. G. Vicidomini, G. Moneron, C. Eggeling, E. Rittweger and S. W. Hell, *Optics Express*, 2012, **20**, 5225-5236.
15. E. Ronzitti, B. Harke and A. Diaspro, *Optics Express*, 2013, **21**, 210-219.
16. I. Coto Hernàndez, C. Peres, F. Cella Zanacchi, M. d'Amora, S. Christodoulou, P. Bianchini, A. Diaspro and G. Vicidomini, *Journal of Biophotonics*, 2014, **7**, 376-380.
17. M. Castello, G. Tortarolo, I. Coto Hernández, T. Deguchi, A. Diaspro and G. Vicidomini, *Review of Scientific Instruments*, 2017, **88**, 053701.
18. J. Heine, M. Reuss, B. Harke, E. D'Este, S. J. Sahl and S. W. Hell, *Proceedings of the National Academy of Sciences*, 2017, **114**, 9797-9802.
19. G. Vicidomini, G. Moneron, K. Y. Han, V. Westphal, H. Ta, M. Reuss, J. Engelhardt, C. Eggeling and S. W. Hell, *Nature Methods*, 2011, **8**, 571-573.
20. J. R. Moffitt, C. Osseforth and J. Michaelis, *Optics Express*, 2011, **19**, 4242-4254.
21. G. Vicidomini, A. Schönle, H. Ta, K. Y. Han, G. Moneron, C. Eggeling and S. W. Hell, *PloS one*, 2013, **8**, e54421.
22. L. Lanzanò, I. Coto Hernández, M. Castello, E. Gratton, A. Diaspro and G. Vicidomini, *Nature communications*, 2015, **6**, 1-9.
23. Y. Sun, G. Tortarolo, K.-W. Teng, Y. Ishitsuka, U. C. Coskun, S.-C. J. Liao, A. Diaspro, G. Vicidomini, P. R. Selvin and B. Barbieri, 2017.
24. L. Wang, B. Chen, W. Yan, Z. Yang, X. Peng, D. Lin, X. Weng, T. Ye and J. Qu, *Nanoscale*, 2018, **10**, 16252-16260.
25. M. A. Digman, V. R. Caiolfa, M. Zamai and E. Gratton, *Biophysical journal*, 2008, **94**, L14-L16.
26. G. Tortarolo, Y. Sun, K. W. Teng, Y. Ishitsuka, L. Lanzanó, P. R. Selvin, B. Barbieri, A. Diaspro and G. Vicidomini, *Nanoscale*, 2019, **11**, 1754-1761.
27. Y. Ma, Y. Lee, C. Best-Popescu and L. Gao, *Proceedings of the National Academy of Sciences*, 2021, **118**, e2004176118.
28. Y.-I. Chen, Y.-J. Chang, S.-C. Liao, T. D. Nguyen, J. Yang, Y.-A. Kuo, S. Hong, Y.-L. Liu, H. G. Rylander, S. R. Santacruz and H.-C. Yeh, *Communications Biology*, 2022, **5**, 1-11.
29. R. Moussavi-Baygi, Y. Jamali, R. Karimi and M. R. Mofrad, *PLoS Computational Biology*, 2011, **7**, e1002049.
30. I. Goodfellow, J. Pouget-Abadie, M. Mirza, B. Xu, D. Warde-Farley, S. Ozair, A. Courville and Y. Bengio, 2014.
31. M. Arjovsky, S. Chintala and L. Bottou, 2017.
32. M. J. Sarmento, M. Oneto, S. Pelicci, L. Pesce, L. Scipioni, M. Faretta, L. Furia, G. I. Dellino, P. G. Pelicci and P. Bianchini, *Nature communications*, 2018, **9**, 1-11.
33. H. Wang, Y. Rivenson, Y. Jin, Z. Wei, R. Gao, H. Günaydın, L. A. Bentolila, C. Kural and A. Ozcan, *Nature Methods*, 2019, **16**, 103-110.
34. C. Bouchard, T. Wiesner, A. Deschênes, F. Lavoie-Cardinal and C. Gagné, *bioRxiv*, 2021.
35. F. Cutrale, V. Trivedi, L. A. Trinh, C.-L. Chiu, J. M. Choi, M. S. Artiga and S. E. Fraser, *Nature Methods*, 2017, **14**, 149-152.
36. S. Ranjit, L. Malacrida, D. M. Jameson and E. Gratton, *Nature protocols*, 2018, **13**, 1979-2004.
37. P. Wang, F. Hecht, G. Ossato, S. Tille, S. Fraser and J. Junge, *Biomedical Optics Express*, 2021, **12**, 3463-3473.
38. I. W. Selesnick, R. G. Baraniuk and N. C. Kingsbury, *IEEE Signal Processing Magazine*, 2005, **22**, 123-151.
39. S. Pelicci, G. Tortarolo, G. Vicidomini, A. Diaspro and L. Lanzanò, *Journal of Physics D: Applied Physics*, 2020, **53**, 234003.
40. L. Wang, Y. Chen, Y. Guo, W. Xie, Z. Yang, X. Weng, W. Yan and J. Qu, *Nano Research*, 2022, **15**, 3479-3486.
41. S. J. Pan and Q. Yang, *IEEE Transactions on Knowledge and Data Engineering*, 2009, **22**, 1345-1359.
42. I. C. Hernàndez, M. d'Amora, A. Diaspro and G. Vicidomini, *Laser Physics Letters*, 2014, **11**, 095603.
43. B. Neupane, T. Jin, L. F. Mellor, E. G. Loboa, F. S. Ligler and G. Wang, *Sensors*, 2015, **15**, 24178-24190.
44. J. Bückers, D. Wildanger, G. Vicidomini, L. Kastrup and S. W. Hell, *Optics Express*, 2011, **19**, 3130-3143.
45. M. Gonzalez Pisfil, I. Nadelson, B. Bergner, S. Rottmeier, A. W. Thomae and S. Dietzel, *Scientific reports*, 2022, **12**, 1-15.
46. C. Wang, M. Taki, Y. Sato, Y. Tamura, H. Yaginuma, Y. Okada and S. Yamaguchi, *Proceedings of the National Academy of Sciences*, 2019, **116**, 15817-15822.
47. X. Yang, Z. Yang, Z. Wu, Y. He, C. Shan, P. Chai, C. Ma, M. Tian, J. Teng and D. Jin, *Nature communications*, 2020, **11**, 1-9.
48. M. S. Frei, M. Tarnawski, M. J. Roberti, B. Koch, J. Hiblot and K. Johnsson, *Nature Methods*, 2022, **19**, 65-70.
49. M. Glogger, D. Wang, J. Kompa, A. Balakrishnan, J. Hiblot, H.-D. Barth, K. Johnsson and M. Heilemann, *ACS Nano*, 2022, **16**, 17991-17997.

